Nonlinear interactions in turbulent jets

Akhil Nekkanti [*]
California Institute of Technology, Pasadena, CA USA

Ethan Pickering
Bayer Crop Science, Boston, MA, USA

Oliver T. Schmidt [†]
University of California San Diego, La Jolla, CA, USA

Tim Colonius [‡]
California Institute of Technology, Pasadena, CA, USA

Bispectral mode decomposition is used to investigate triadic interactions within a Mach 0.4 turbulent jet. We explore its potential to identify dominant triadic interactions and their associated spatial structures in an unforced turbulent jet. The bispectral measure is broadband in frequency for each azimuthal wavenumber triad. The [1,1,2] and [0,0,0] azimuthal wavenumber triads are dominant, emphasizing the importance of the self-interactions of the helical and axisymmetric components. Bispectral modes reveal that streaky structures are fed by the interaction of a Kelvin-Helmholtz wavepacket with its conjugate. Streaks are also observed in other frequency interactions, occurring in regions where the structures of these frequencies are spatially active. Furthermore, integral interaction maps and nonlinear transfer terms are computed to determine the direction of energy transfer and to pinpoint the spatial regions where nonlinearity is most active. As the shear layer develops, small scales interact nonlinearly, transferring energy to larger scales. Moving downstream, near the potential core closure, larger scales become more active, resulting in a forward energy cascade.

I. Introduction

In turbulent jets, coherent structures are the primary sources of aft-angle noise [1]. The pioneering work by Crow and Champagne [2] identified the presence of large-scale coherent structures in turbulent jets. Subsequent researchers [3–7] have modeled these coherent structures as linear stability solutions of the turbulent mean flow. Most studies, until now, have focused on characterizing these structures in terms of their statistical importance and have linked them to linear mechanisms [8–10]. In this work, our emphasis is on identifying the nonlinear triadic interactions and their associated spatial structures.

Quadratic nonlinearities arise from the convective term of the Navier-stokes equation, which leads to three-wave coupling or triadic interactions. A triad is a set of three wavenumbers (or frequencies) that form a triangle, i.e., they satisfy the following condition

$$\mathbf{k} \pm \mathbf{p} \pm \mathbf{q} = 0, \tag{1}$$
$$f_1 \pm f_2 \pm f_3 = 0. \tag{2}$$

These triadic interactions play a vital role in the energy cascade of turbulent flows [11–13]. Researchers have employed bispectral analysis to study these interactions [14–17]. The bispectrum, an extension of the power spectrum to third order, is calculated through a double Fourier transform of third-order moments. It measures the quadratic phase coupling only at a single spatial point, thereby characterizing triadic interaction locally. However, our objective extends beyond this local analysis; we aim to identify coherent structures associated with triadic interactions. To this end, we employ the bispectral mode decomposition (BMD) proposed by Schmidt [18]. BMD identifies the most dominant triads and their corresponding coherent structures by maximizing the spatially integrated bispectrum. BMD has been used to

---

[*]Postdoctoral Scholar, AIAA Member
[†]Associate Professor, Department of Mechanical and Aerospace Engineering, Senior Member AIAA.
[‡]Frank and Ora Lee Marble Professor of Mechanical Engineering, Mechanical and Civil Engineering, Associate Fellow AIAA

investigate the triadic interactions in various flow configurations, such as laminar-turbulent transition on a flat plate [19, 20], forced jets [21–23], swirling flows [24, 25], bluff body wakes [26], and wake of an airfoil [27].

Nonlinear dynamics in jets have predominantly been studied in two contexts: transitional flows and harmonically forced jets. Transitional flows have been the focus of studies examining the nonlinear interaction between the fundamental and subharmonic wave [28–30]. Meanwhile, studies on forced jets have examined nonlinear effects on mean flow deformation [31, 32], azimuthal symmetry breaking [33, 34] and the formation of periodic and chaotic attractors [35, 36]. Here, our focus is exclusively on non-resonant flows, intending to shed light on the nonlinear wave coupling that is still present, albeit in lower magnitude. Furthermore, we will analyze the direction of energy transfer between different azimuthal wavenumbers. The paper is organized as follows. In section II, the BMD methodology is discussed. Results are presented in section III, and the paper is summarized in section IV.

II. Cross-Bispectral mode decomposition (C-BMD)

We employ the cross-bispectral mode decomposition, recently developed by [18], to identify the spatially coherent structures arising from the triadic interactions in turbulent flows. Here, we provide a brief overview of the method. The reader is referred to Schmidt [18] for further details of the derivation and mathematical properties of the method.

Given a statistically stationary flow field, let $\mathbf{q}_i = \mathbf{q}(t_i)$ denote the mean subtracted snapshots, where $i = 1, 2, \cdots n_t$ are n_t number of snapshots. For spectral estimation, using the Welch's approach the dataset is first segmented into n_{blk} overlapping blocks with n_{fft} snapshots in each block. The neighbouring blocks overlap by n_{ovlp} snapshots with $n_{\text{ovlp}} = n_{\text{fft}}/2$. The n_{blk} blocks are then Fourier transformed in time and all Fourier realizations of the l-th frequency, $\mathbf{q}_l^{(j)}$, are arranged in a matrix,

$$\hat{\mathbf{Q}}_l = \left[\hat{\mathbf{q}}_l^{(1)}, \hat{\mathbf{q}}_l^{(2)}, \cdots, \hat{\mathbf{q}}_l^{(n_{\text{blk}})} \right]. \tag{3}$$

The auto-bispectral matrix is then computed as

$$\mathbf{B} = \frac{1}{n_{\text{blk}}} \hat{\mathbf{Q}}_{k \circ l}^H \mathbf{W} \hat{\mathbf{Q}}_{k+l}, \tag{4}$$

where $\hat{\mathbf{Q}}_{k \circ l}^H = \hat{\mathbf{Q}}_k^* \circ \hat{\mathbf{Q}}_l^*$ and $\mathbf{W}$ is the diagonal matrix containing the spatial quadrature weights. The auto-bispectral density matrix measures the interactions between different frequenices at the same azimuhtal wavenumber. To estimate the interactions between the azimuthal wavenumber triad, $[m_1, m_2, m_3]$, where $m_1 + m_2 = m_3$, we construct the cross-bispectral matrix

$$\mathbf{B}_c = \frac{1}{n_{\text{blk}}} \left(\hat{\mathbf{Q}}_k^* \circ \hat{\mathbf{R}}_l^* \right) \mathbf{W} \hat{\mathbf{S}}_{k+l}. \tag{5}$$

Here, $\hat{\mathbf{Q}}_k, \hat{\mathbf{R}}_l, \hat{\mathbf{S}}_{k+l}$, comprises of all the Fourier realizations at the k-th frequency of the azimuthal wavenumber m_1, the l-th frequency of the azimuthal wavenumber m_2, and the $(k + l)$-th frequency of the azimuthal wavenumber m_3, respectively. Owing to the non-Hermitian nature of the bispectral matrix, the optimal expansion coefficients, $\mathbf{a}_1$ are obtained by maximising the absolute value of the Rayleigh quotient of $\mathbf{B}_c$

$$\mathbf{a}_1 = \arg \max_{\|\mathbf{a}\|=1} \left| \frac{\mathbf{a}^* \mathbf{B}_c \mathbf{a}}{\mathbf{a}^* \mathbf{a}} \right|. \tag{6}$$

The complex mode bispectrum is then obtained as

$$\lambda_1(f_k, f_l) = \left| \frac{\mathbf{a}_1^* \mathbf{B}_c \mathbf{a}_1}{\mathbf{a}_1^* \mathbf{a}_1} \right|. \tag{7}$$

Finally, the leading-order bispectral modes and the cross-frequency fields are recovered as

$$\boldsymbol{\phi}_{k+l}^{(1)} = \hat{\mathbf{S}}_{k+l} \mathbf{a}_1, \quad \text{and} \tag{8}$$

$$\boldsymbol{\phi}_{k \circ l}^{(1)} = \left(\hat{\mathbf{Q}}_k \circ \hat{\mathbf{R}}_l \right) \mathbf{a}_1, \tag{9}$$

respectively. By construction, the bispectral modes and cross-frequency fields have the same set of expansion coefficients. This explicitly ensures the causal relation between the resonant frequency triad, $(f_k, f_l, f_k + f_l)$, where $\hat{\mathbf{Q}}_k \circ \hat{\mathbf{R}}_l$ is the
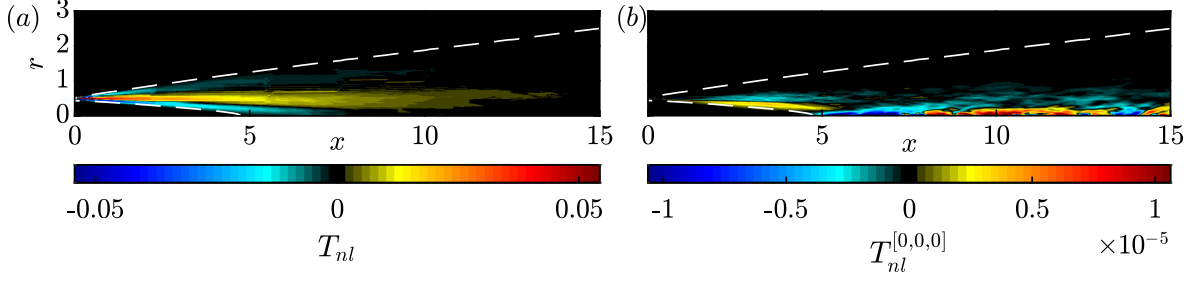
2

Figure 1   **Spatial field of the nonlinear energy transfer:** (*a*) **total;** (*b*) **azimuthal wavenumber triad,** $[m_1, m_2, m_3] = [0, 0, 0]$**.**

cause and $\hat{\mathbf{S}}_{k+l}$ is the effect. The complex mode bispectrum, λ_1, measures the intensity of the triadic interaction and the bispectral mode, $\boldsymbol{\phi}_{k+l}$, represents the structures that results from the nonlinear triadic interaction. Another useful quantity is the interaction map, defined as

$$\boldsymbol{\psi}_{k,l} = |\boldsymbol{\phi}_{k\circ l} \circ \boldsymbol{\phi}_{k+l}|. \tag{10}$$

This interaction map identifies the spatial regions of activity of the triadic interaction for the frequency triad, (f_k, f_l, f_{k+l}) and wavenumber $[m_1, m_2, m_3]$. In this study, we differentiate between the frequency and azimuthal wavenumber triads using the notation $(\cdot, \cdot, \cdot)$ and $[\cdot, \cdot, \cdot]$, respectively.

III. Results

The large eddy simulation (LES) data of an isothermal subsonic turbulent jet, at a Mach number $M_j = U_j/c_\infty = 0.4$ and a Reynolds number $Re = \rho_j U_j D/\mu_j = 450,000$ computed by Brès and Lele [37] is considered. Here, ρ is the density, U velocity, D nozzle diameter, μ dynamic viscosity and c speed of sound. The simulations were carried out using the compressible flow solver 'Charles' on an unstructured grid using a finite-volume method. The reader is referred to [38, 39] for further details on the numerical method, meshing, and subgrid-models. The LES database consists of 20000 snapshots sampled at an interval of $\Delta t c_\infty/D = 0.2$ acoustic time units. Data interpolated on a cylindrical grid spanning $x, r \in [0, 30] \times [0, 6]$ was used in this analysis. The flow is non-dimensionalized by the nozzle exit values, namely velocity by U_j, pressure by $\rho_j U_j^2$, length by the nozzle diameter D, and time by D/U_j. Frequencies are reported in terms of the Strouhal number $St = f D/U_j$. We focus our analysis to the most energetic wavenumbers, $m = 0, 1, 2, 3, 4$, and frequencies, $St_3 \in [-2, 2]$, within the domain $x/D \in [0, 20]$ and $r/D \in [0, 3]$. The higher wavenumbers and frequencies are important near the nozzle's exit and will be considered wherever relevant.

Quadratic nonlinearities arise from the convective term in the Navier-Stokes equation. Corresponding they contribute to the turbulent kinetic energy through the nonlinear transport term [40] given by:

$$T_{nl} = -\frac{1}{2} \frac{\partial}{\partial x_i} \overline{u_i' u_j' u_i'}. \tag{11}$$

The nonlinear energy transfer for an azimuthal wavenumber triad, $[m_1, m_2, m_3]$, is given as

$$T_{nl}^{[m_1, m_2, m_3]} = -\mathcal{R} \left[\overline{\hat{u}_j^*(m_3) \hat{u}_i(m_1) \frac{\partial \hat{u}_j}{\partial x_i}(m_2)} \right]. \tag{12}$$

Figure 1 shows the spatial field for the total nonlinear transfer and the wavenumber triad [0,0,0]. Red and blue colors represent positive and negative energy transfer from the mean flow to the fluctuations. The total nonlinear energy transfer, T_{nl}, reveals that all nonlinear interactions occur in the shear layer and are concentrated around the lip line ($r = 0.5$) within the first five jet diameters. On the other hand, the nonlinearity generated due to the self-interaction of the axisymmetric component is concentrated near the centerline beyond the end of the potential core. Later, in figure 4, we will demonstrate that the nonlinear activity near the nozzle's exit is due to higher wavenumber interactions, and the nonlinear activity at the end of the potential core results from interactions between lower azimuthal wavenumbers.

We now perform BMD to identify the dominant triadic interactions. BMD is computed for blocks containing $n_{\text{fft}} = 256$ snapshots with 50% overlap, resulting in a total number of $n_{\text{blk}} = 158$ blocks. For best practices on spectral
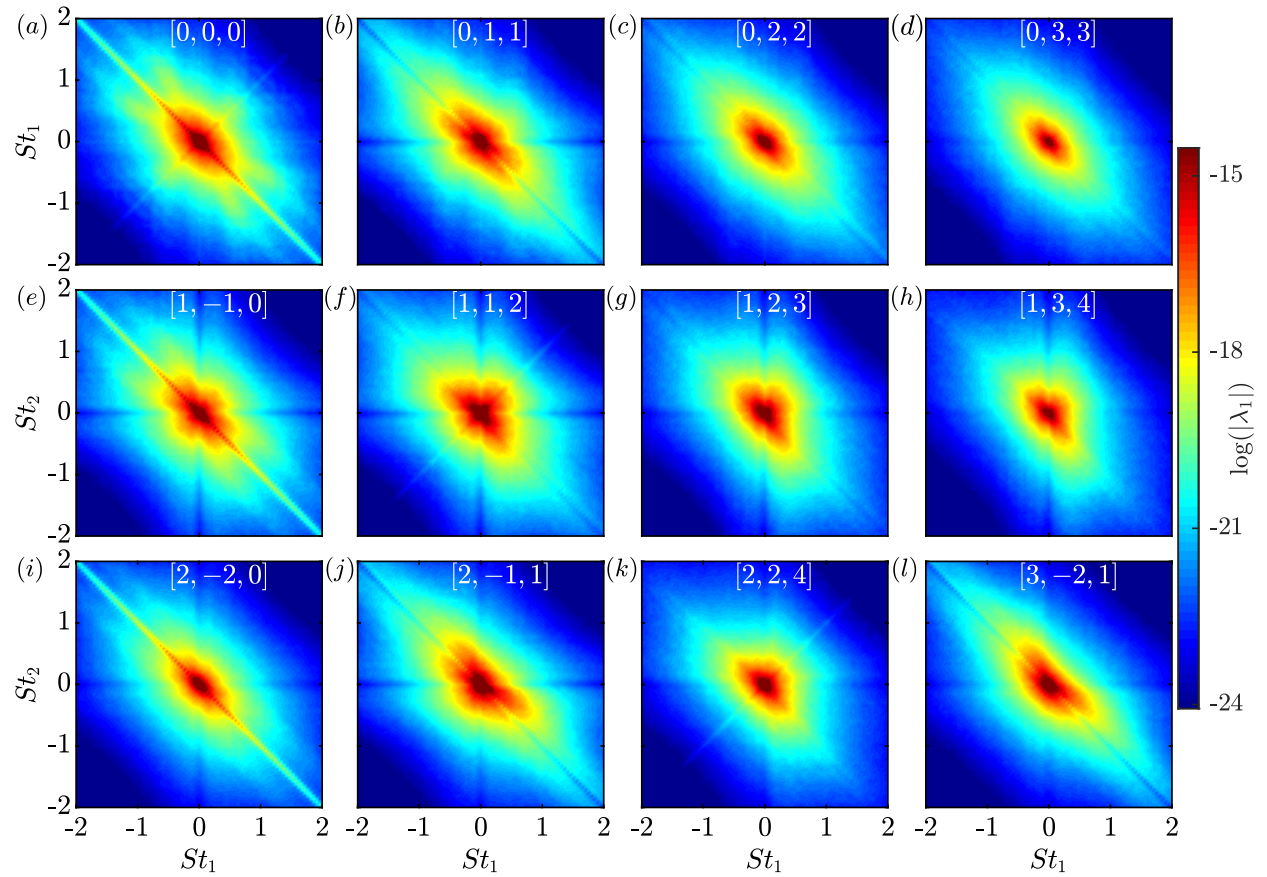
3

Figure 2   Cross-bispectra of twelve azimuthal wavenumber triads, $[m_1, m_2, m_3]$. Here the magnitude of the complex cross-bispectral measure, $|\lambda_1|$, is presented.
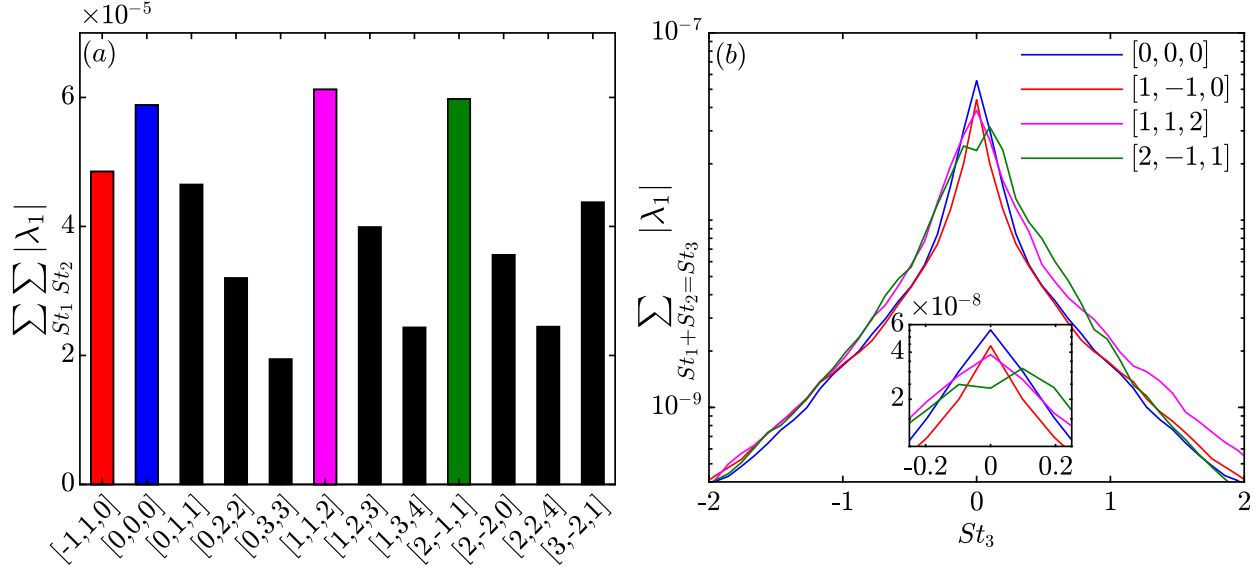
4

Figure 3 **Cross-bispectra summed by magnitude:** (*a*) **over all frequency triads;** (*b*) **over diagonals of slope -1 such that** $St_1 + St_2 = St_3$**.**

estimation parameters, we refer to [41–44]. The cross-bispectra for twelve dominant azimuthal triads are shown in 2. The high-intensity regions (false red color) signify the dominant triads that arise from the interactions of two frequencies. All twelve cases exhibit broadband behavior, with the most intense interactions occurring at low frequencies. Similarly, in the wavenumber space, the intensity decreases for higher azimuthal wavenumber interactions, as seen in [0,3,3], [1,3,4], and [2,2,4]. A band is observed along $St_3 = 0$ for [0,0,0], [1,-1,0], and [2,-2,0] triads, which is due to spectral leakage, and caution is advised while making interpretations. The cross-bispectrum for the azimuthal triads, [0,0,0], [1,-1,0] and [2,-2,0] exhibit a four-fold symmetry about the lines, $St_1 = St_2$ and $St_1 = -St_2$, whereas the azimuthal triads [1,1,2] and [2,2,4] are symmetric about the line $St_1 = St_2$. Other triads triads do not exhibit any obvious symmetries.

Figure 3 shows the cross-bispectrum summed over all frequency triads and summed over diagonals of slope -1 such that $St_1 + St_2 = St_3$. The former represents the total intensity of triadic interactions for a single azimuthal wavenumber triad, while the latter denotes the intensity of the resulting frequency for a single wavenumber triad. Figure 3(*a*) reveals that the four dominant azimuthal wavenumber triads are [1, 1, 2], [0, 0, 0], [2, −1, 1], and [−1, 1, 0]. The self-interaction of $m = 1$ resulting in $m = 2$ is the most significant triad. This is expected since $m = 1$ and $m = 2$ are the most energetic components [45], and hence their triadic interaction results in the greatest cross-bispectra values. The cross-bispectra, summed along diagonals, are shown in figure 3(*b*) for the four dominant wavenumber triads. The four curves decrease monotonically and exhibit behavior reminiscent of broadband nature. The triads [0,0,0], [1,-1,0], [1,1,2] peak at $St_3 \to 0$, whereas [2,-1,1] peaks at the first non-zero frequency, $St_3 \approx 0.05$, as shown in the inset of figure 3(*b*). Another interesting observation is that the summed cross-bispectrum is not symmetric about $St_3 = 0$ because $\mathbf{q}_{m,f_1} \neq \mathbf{q}_{m,-f_1}$ when $m > 0$. For $St_3 \geqslant 1$, the triad [1,1,2] exhibits the largest values, indicating that the strongest triadic interactions lead to the azimuthal wavenumber $m = 2$ within this frequency range.

Next, we identify the regions where triadic interactions are most active. To achieve this, the weighted interaction maps are summed over all frequency triads as $\sum_{k,l} \lambda_1(St_k, St_l)|\phi_{k \circ l} \circ \phi_{k+l}|$. Figure 4 shows the weighted interaction maps for six azimuthal wavenumber triads. The top row highlights three out of the four dominant wavenumber triads, while the bottom row illustrates interactions resulting in higher azimuthal wavenumbers. For dominant triads, the triadic interactions are present in the shear layer and beyond the end of the potential. The region of nonlinear activity extends farthest downstream for the [0,0,0] triad. Our findings are in agreement with Tissot et al. [46], demonstrating that nonlinearity becomes pronounced downstream of the potential core's end for the axisymmetric component. In the case of interactions involving higher azimuthal wavenumbers, the region of nonlinear activity shifts upstream, closer to the nozzle's exit. This reiterates our observation from figure 1 that interactions of higher wavenumbers play a more significant role in the nonlinearities closer to the nozzle's exit.

Figure 5 displays the interaction maps for six representative frequency triads of the most dominant azimuthal
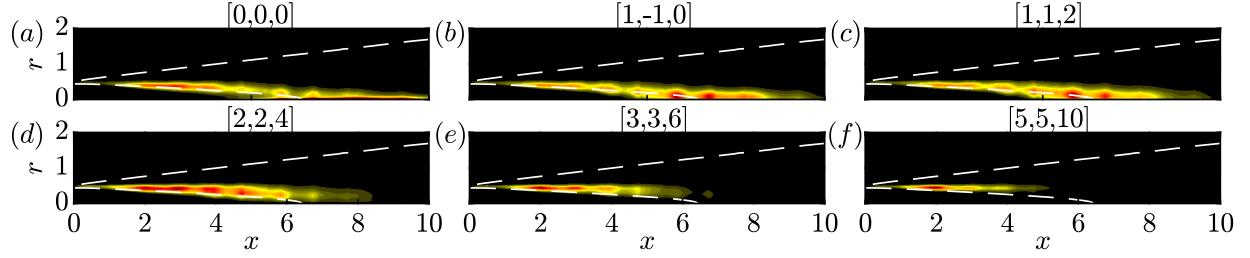
5

Figure 4 **Integral interaction maps,** $\sum_{k,l} \lambda_1(St_k, St_l)|\phi_{k \circ l} \circ \phi_{k+l}|$, **for azimuthal triads,** $[m_1, m_2, m_3]$**:** (*a*) **[0,0,0];** (*b*) **[1,-1,0];** (*c*) **[1,1,2];** (*d*) **[1,2,3];** (*e*) **[2,2,4];** (*f*) **[5,5,10].**
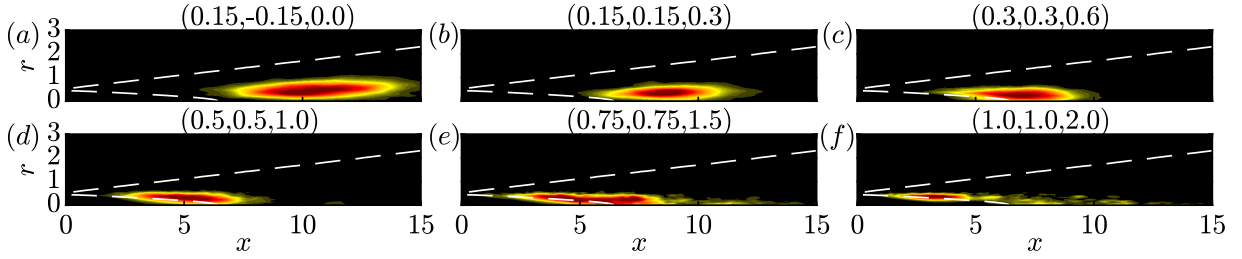

Figure 5 **Interaction maps,** $|\phi_{k \circ l} \circ \phi_{k+l}|$, **of the azimuthal wavenumber triad [1,1,2] for different frequency triads,** (St_1, St_2, St_3)**:** (*a*) **(0.15,-0.15,0.0);** (*b*) **(0.15,0.15,0.0);** (*c*) **(0.3,0.3,0.0);** (*d*) **(0.5,0.5,1.0);** (*e*) **(0.75,0.75,1.5);** (*f*) **(1.0,1.0,2.0).**

wavenumber triad [1,1,2]. This figure highlights the regions where nonlinear interactions are most active in frequency space, contrasting with the wavenumber space shown in Figure 4. The interaction maps indicate that nonlinear interactions between lower frequencies occur downstream. In contrast, for interactions involving higher frequencies, this region of nonlinearity shifts upstream, closer to the nozzle's exit. Overall, figures 4 and 5 indicate that the small-scale structures are active upstream and large-scale structures are active downstream. This observation is not surprising, as due to the spreading of the shear layer, structures with larger wavelengths are supported farther downstream than those associated with smaller wavelengths.

A. Role of triadic interactions in the formation of streaks

Figure 6 shows the bispectral modes due to the interaction between $m = \pm1$, $St = \pm0.3$, leading to four possible interactions: (i) $[1, 1, 2]$, $(0.3, 0.3, 0.6)$; (ii) $[1, 1, 2]$, $(0.3, -0.3, 0.0)$; (iii) $[1, -1, 0]$, $(0.3, 0.3, 0.6)$;(iv) $[1, -1, 0]$,
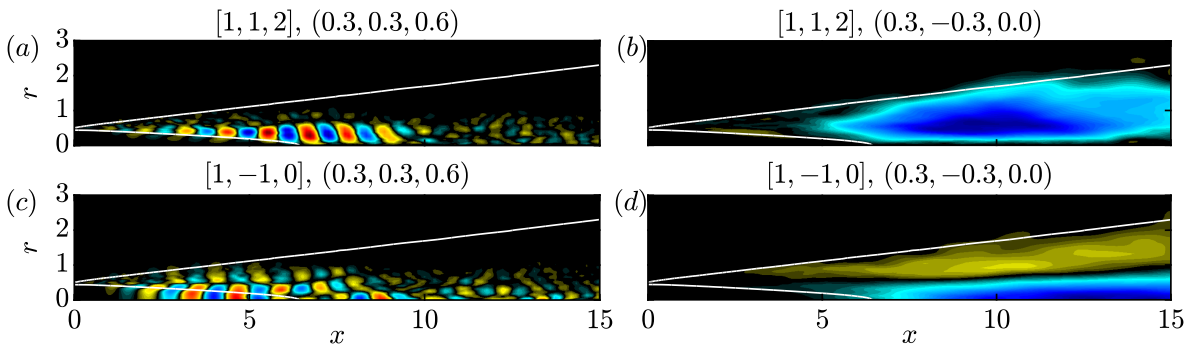

Figure 6 **Real component of the fluctuating streamwise velocity of the cross-bispectral mode for three frequency triads and three azimuthal wavenumber triads. Top (*a*,*b*) and bottom (*c*,*d*) rows show the azimuthal wavenumber triads** $[1, 1, 2]$**, and** $[1, -1, 0]$**, respectively. The left and right columns depict the frequency triads,** $(0.3, 0.3, 0.6)$**, and** $(0.3, -0.3, 0.0)$**, respectively. Contours (■■■) are given by** $\pm||\phi_1 : u_x||_\infty$ **of each mode.**

6

$(0.3, -0.3, 0.0)$. We specifically chose $m = \pm 1$ and $St = \pm 0.3$ because it exhibits the largest resolvent gain [45]. In both azimuthal wavenumber triads, constructive self-interference of $St = 0.3$ generates structures resembling KH wavepackets, while destructive self-interaction of $St = 0.3$ produces elongated structures localized beyond the end of the potential core. Notably, the structure in figure 6(b) resembles a large-scale streaky structure, suggesting that the KH mode of $m = 1, St = 0.3$ interacts with its conjugate $m = 1, St = -0.3$, giving rise to streaks. These observations are inline with a number of previous studies in free shear flow and jets that have postulated the creation of vortices, that ultimately give rise to streaks, via the interaction of KH modes ([32, 47, 48].
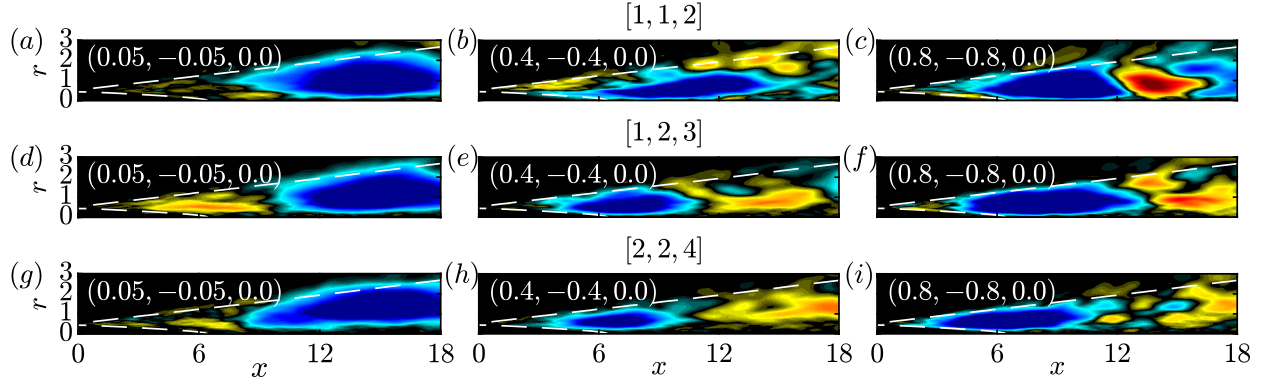

Figure 7 Real component of the fluctuating streamwise velocity of the cross-bispectral mode for three frequency triads and three azimuthal wavenumber triads. Top (*a-c*), middle (*d-f*), and bottom (*g-i*) rows show the azimuthal wavenumber triads $[1, 1, 2]$, $[1, 2, 3]$ and $[2, 2, 4]$, respectively. The left, center, and right columns depict the frequency triads, $(0.05, -0.05, 0.0)$, $(0.4, -0.4, 0.0)$, and $(0.8, -0.8, 0.0)$, respectively. Contours (▬▬) are given by $\pm 0.5 ||\phi_1 : u_x||_\infty$ of each mode.

We further investigate the role of triadic interactions in the formation of streaks. Figure 7 shows the bispectral modes for three azimuthal wavenumber triads: $[1, 1, 2]$, $[1, 2, 3]$, and $[2, 2, 4]$, and three frequency triads: $(0.05, -0.05, 0.0)$, $(0.4, -0.4, 0.0)$, and $(0.8, -0.8, 0.0)$. Streaks are azimuthally non-uniform structures and are not present in the axisymmetric component ($m = 0$). Additionally, Pickering et al. [49] demonstrated that $m = 2, 3$, and 4 are the most significant contributors to streaks. Therefore, we choose the dominant azimuthal triads, which results in these wavenumbers. All nine modes display an elongated region in blue false color, indicating the presence of streaks. Streaks are located beyond the end of the potential core for interactions at lower frequencies, while at higher frequencies, they appear at a more upstream location. Similarly, higher azimuthal wavenumbers triads generate streaks at a more upstream location. This finding is in accordance with Pickering et al. [49], where they show that the most energetic azimuthal wavenumber contributing to streaks scales as $m_{max} \sim 1/x + 1$.
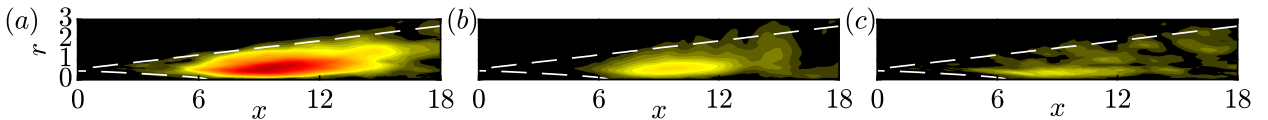

Figure 8 Magnitude of three velocity components of the cross-bispectral mode for the frequency triad, (0.4,-0.4,0.0) and the wavenumber triad, [1,1,2]: (*a*) u_x; (*b*) u_r; (*c*) u_θ.

A salient feature of the streaky structures is that the amplitude of the streamwise velocity is significantly higher than the radial and azimuthal velocities. To confirm this, the magnitude of the velocity components for the bispectral mode corresponding to the wavenumber triad, $[1, 1, 2]$, and frequency triad $(0.4, -0.4, 0.0)$ are shown in figure 8. It is clear that the magnitude of the streamwise velocity is greater, quantitatively by a factor of 3, than the other two velocity components. This confirms that the structures in figure 7 are indeed streaks.

In turbulent wall-bounded flows, the generation of streaks through the lift-up mechanism is widely accepted [50–52]. This mechanism entails counter-rotating vortices elevating the low-speed fluid while bringing down the high-speed

fluid, leading to streak formation. Recent studies by Pickering et al. [49], Nogueira et al. [53] have demonstrated the existence of a lift-up mechanism in jets as well. Lift-up is considered a linear non-modal mechanism, here, we consider the effect of nonlinearity. The linear non-modal instability assumes an inviscid, incompressible, parallel flow, i.e., $\mathbf{U} = (U, V, W) = (U(r), 0, 0)$. By linearizing the momentum equations, we obtain,

$$\frac{\partial u_x}{\partial t} + u_r \frac{\partial U}{\partial r} = 0 \tag{13}$$

On including the nonlinear terms, this is modified to

$$\frac{\partial u_x}{\partial t} + u_r \frac{\partial U}{\partial r} + u_i \frac{\partial u_x}{\partial x_i} = 0, \tag{14}$$

where u_i is the fluctuating velocity, and U is the temporally averaged mean flow. Left multiplying by u_x^* and taking the temporal mean gives

$$\frac{\partial \overline{|u_x|^2}}{\partial t} = -\overline{u_x^* u_r \frac{\partial U}{\partial r}} - \overline{u_x^* u_i \frac{\partial u_x}{\partial x_i}}. \tag{15}$$

This equation reveals that shear production and the nonlinear transfer contribute to the intensity of streaks, whereas in the absence of nonlinearity, shear production is the only contributor. For the streak mode corresponding to $m = 2, St = 0$, equation (15) becomes

$$\frac{\partial \overline{|\hat{u}_x|^2}}{\partial t} = -\mathcal{R} \left[\underbrace{\overline{\hat{u}_x^* \hat{u}_r \frac{\partial U}{\partial r}}}_{P_{xr}} + \underbrace{\overline{\hat{u}_x^* u_i \frac{\widehat{\partial u_x}}{\partial x_i}}}_{T_{x-nl}} \right]_{(m=2,St=0)} . \tag{16}$$

where $\mathcal{R}$ denotes the real part, P_{xr} and T_{x-nl} represent the shear production and the nonlinear transfer term contributing to the intensity of streamwise velocity.
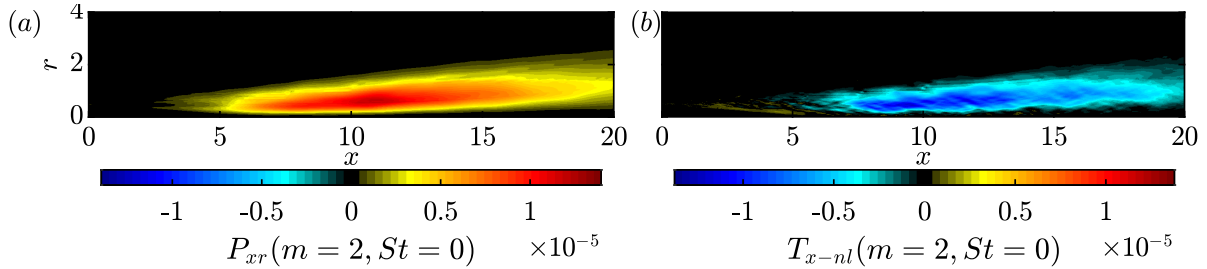

Figure 9 **Contribution of the shear production** (a) **and nonlinear transfer** (b) **to the streaky structures in** $m = 2$.

Figure 9 illustrates the contribution of shear production and the nonlinear term to the intensity of the streamwise velocity for the streak mode at $m = 2$. We observe that the magnitudes of the nonlinear and linear terms, i.e., shear production, are similar. However, these terms have opposite signs, suggesting that shear production supplies energy to the streaky structures, while nonlinearities extract energy from them. This figure reveals that nonlinear interactions also play a significant role in streak formation and the corresponding lift-up mechanism, highlighting the need for their consideration in future studies.

B. Energy cascade

Figure 10 shows the normalized turbulent kinetic energy (TKE) and bispectrum as a function of streamwise location. The TKE is computed at each spatial location and then integrated radially for each azimuthal wavenumber. The bispectrum is computed by performing BMD on different streamwise planes. Finally, at each streamwise location, the TKE and bispectrum are normalized by total TKE and total bispectrum, $\sum_{m,St} b(x, m, St)$. A similar trend is observed for both the TKE and bispectrum. Near the nozzle exit, higher azimuthal wavenumbers are more energetic and exhibit greater triadic activity. As the flow evolves downstream, the energy and bispectral measure is concentrated at lower azimuthal wavenumbers. The similar trend observed between figure 10(a) and (b) suggests that the azimuthal
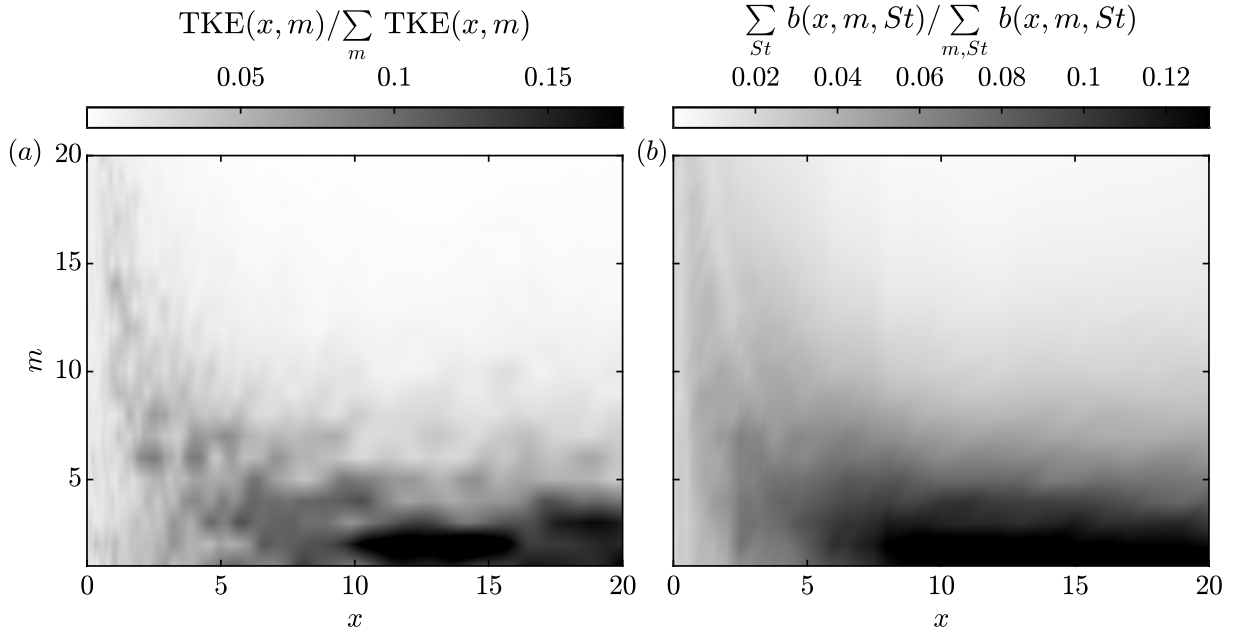
8

Figure 10   Normalized TKE (*a*) and bispectrum (*b*) as a function of streamwise location and azimuthal wavenumber.

wavenumber involved in the strongest nonlinear interactions is also the most energetic. Previous studies [9, 54, 55] show that the frequency of the dominant wavepackets scales as $1/x$. Analogously, we observe that the most dominant azimuthal wavenumber decreases with x.

We now examine which azimuthal triads are dominant at different streamwise locations in figure 11. These are identified by calculating the spatial triple correlation of velocity components for different azimuthal wavenumber triplets, averaging over time, and selecting the triads with the highest values. The circle size represents the intensity of the triad. The dotted line in magenta denotes the most energetic azimuthal wavenumber. Here, we do not focus on the triad [0,0,0] in our analysis, as it does not offer insights into either inverse or forward energy cascades. The top and bottom rows represent the spatial locations before and after the end of the potential core, respectively. At $x = 1$, $m = 12$ is the most energetic component, and the strongest triad is [6,6,12] (excluding the [0,0,0] triad). As in figure 10, this suggests that the most energetic wavenumber is also involved in the dominant nonlinear interactions. Moving downstream, the strongest azimuthal triad transitions to [3, 3, 6] at $x = 2$, [2, 2, 4] at $x = 3$, [1, 1, 2] at $x = 5$, and 7. For $x \geqslant 10$, the dominant azimuthal triads are [4, -2, 2] and [2, 2, 4]. At all spatial locations, we observe that the most dominant triads are of the form $[m, m, 2m]$ and $[2m, -m, m]$. The former represents a forward energy cascade, whereas the latter denotes an inverse energy cascade. In the initial shear layer, the shift in the dominant triad from higher to lower azimuthal components suggests an inverse energy cascade, and the increase from [1, 1, 2] to [2, 2, 4] beyond $x = 10$ suggests a forward energy cascade.

Next, the direction of energy transfer between the dominant triads of figure 11 is investigated. Figure 12 shows the nonlinear energy transfer, T_{nl}, for the six triads, $[12, -6, 6]$, $[6, -3; 3]$, $[4, -2, 2]$, $[6, 6, 12]$, $[3, 3, 6]$, and $[2, 2, 4]$. For a triad $[m_1, m_2, m_3]$, the red color denotes the energy transfer from m_1 and m_2 to m_3 and the blue color denotes the energy extracted from m_3 by m_1 and m_2. The spatial fields in the top row display a region of positive nonlinear transfer, followed by a region of negative energy transfer. In contrast, the energy transfer patterns in the bottom row are opposite to those in the top row. However, both rows convey the same information. For example, the spatial field corresponding to the $[12, -6, 6]$ triad demonstrates energy transfer from $m = 12, -6$ to 6 until $x \approx 2.8$, after which there is a backscatter of energy from $m = 6$ to $m = 12$. Similarly, the $[6, 6, 12]$ triad indicates that initially, $m = 6$ extracts energy from $m = 12$, but later, the energy transfers from $m = 6$ to $m = 12$. The triads in the middle and right columns exhibit similar trends. These observations clearly show that the inverse energy cascade is active in the initial shear layer, while the forward energy cascade becomes prominent at more downstream locations.

Most of the studies that have investigated the presence of the inverse energy cascade have been conducted in isotropic
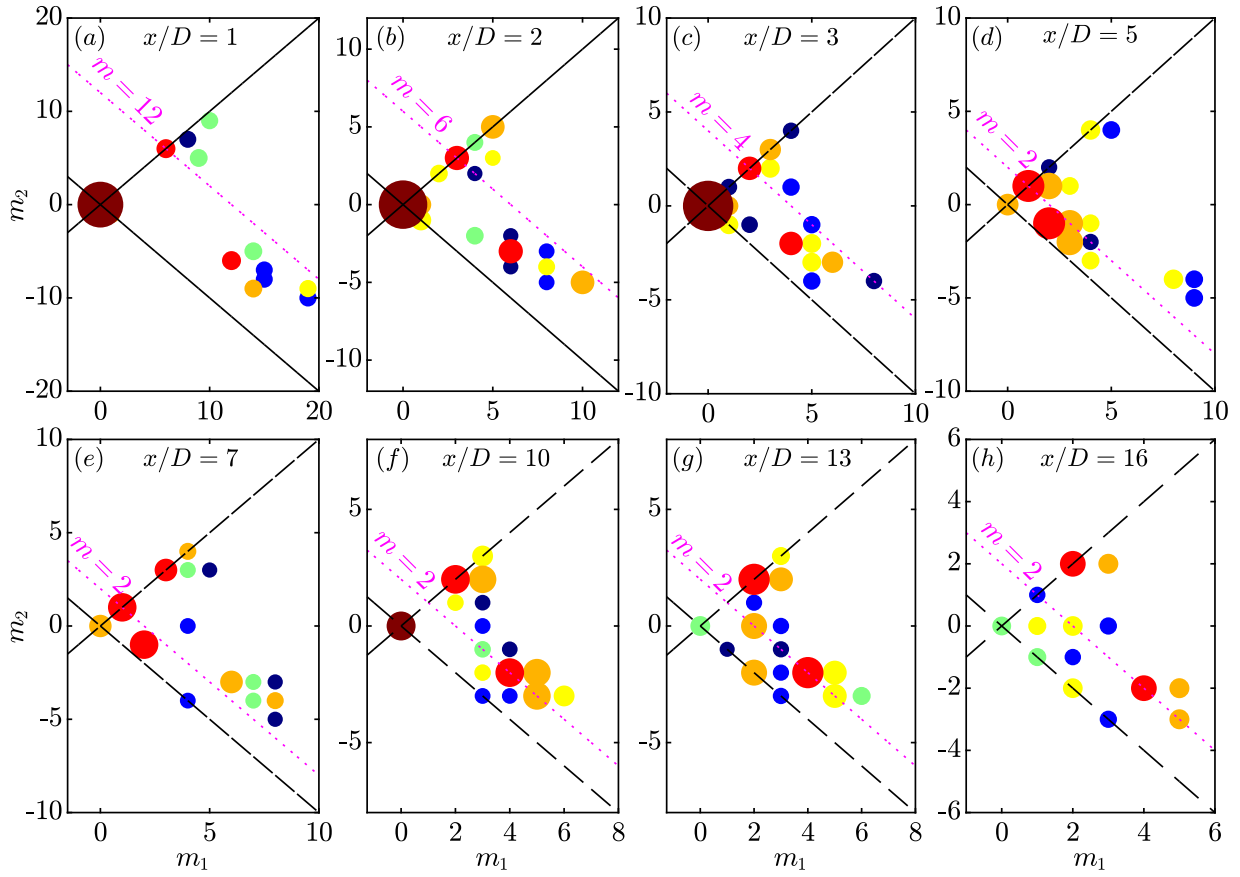
9

Figure 11   Dominant azimuthal triads at different spatial locations: (*a*) $x/D = 1$; (*b*) $x/D = 2$; (*c*) $x/D = 3$; (*d*) $x/D = 5$; (*e*) $x/D = 7$; (*f*) $x/D = 10$; (*g*) $x/D = 13$; (*h*) $x/D = 16$.
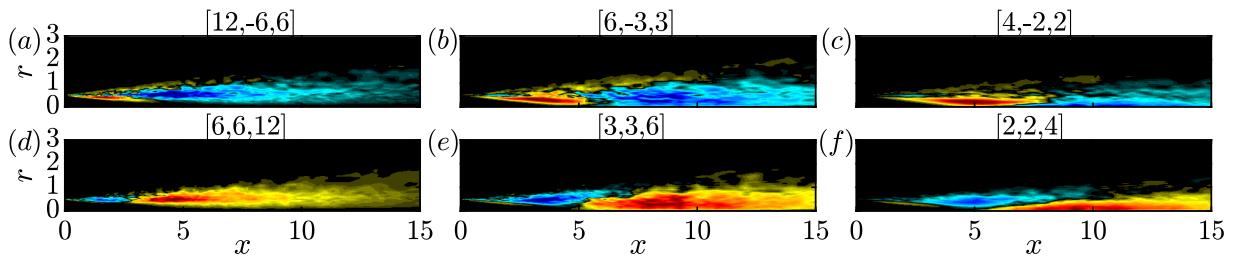

Figure 12   Nonlinear transfer fields for different azimuthal triads, [m_1, m_2, m_3]: (*a*) $[12, -6, 6]$; (*b*) $[6, -3; 3]$; (*c*) $[4, -2, 2]$; (*d*) $[6, 6, 12]$; (*e*) $[3, 3, 6]$; (*f*) $[2, 2, 4]$. **Contours (■■) are given by** $-0.5 \leqslant T_{nl}/\|T_{nl}\|_\infty \leqslant 0.5$ **of each field.**
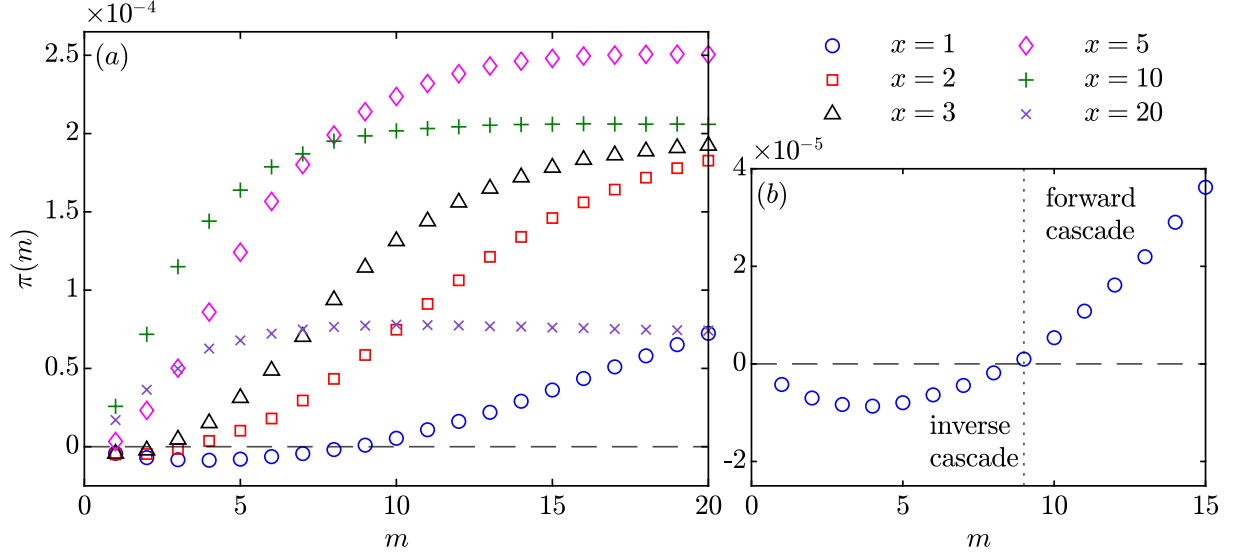
Figure 13   Rate for energy transfer, $\pi(m)$, from the first m azimuthal wavenumbers to higher m at different streamwise locations. An enlarged view of (a) at $x = 1$ is shown in (b).

turbulent flows, for example [56–58]. To quantify the energy transfer, following Plunian et al. [59], we use the metric

$$\pi(m) = \sum_{|m'| \leqslant m} \mathcal{R}\left[\overline{(\hat{\mathbf{u}}(m'))^* \mathcal{F}[\mathbf{u} \cdot \nabla\mathbf{u}](m')}\right] \tag{17}$$

where, $\mathcal{F}[\cdot]$ denotes the Fourier transform. This metric represents the rate of energy transferred by the first m wavenumbers to wavenumbers greater than m. A positive value of $\pi(m)$ indicates a forward cascade, where energy is transferred from larger to smaller scales, while a negative value indicates an inverse cascade, where energy moves from smaller to larger scales. Figure 13 illustrates the rate of energy transfer at various spatial locations. Near the nozzle's exit in the streamwise direction, there is an inverse energy cascade for lower azimuthal wavenumbers and a forward energy cascade for higher azimuthal components. However, at more downstream locations, only a forward energy cascade is observed, consistent with Figure 12. In figure 13 (b), a zoomed-in view of $\pi(m)$ at $x = 1$ reveals that wavenumbers $m \leqslant 9$ gain energy through the inverse cascade.

IV. Summary and Conclusions

In this study, the nonlinear interactions in a Mach 0.4 turbulent jet were analyzed for various frequency triads and azimuthal wavenumber triads using BMD. The mode bispectrum exhibits a broadband-like nature for all azimuthal wavenumber triads. The most significant azimuthal wavenumber triads are [1,1,2] and [0,0,0], indicating that the most energetic wavenumbers are also engaged in the most intense triadic interactions. BMD modes demonstrated the presence of streaks in the [1,1,2] triad. In particular, the KH-wavepacket at $m = 1, St = 0.3$ interacts with its conjugate at $m = 1, St = -0.3$ to generate streaks. Streaks were also observed at other frequency- and wavenumber-triads, implying that nonlinear interactions contribute to their formation. For interaction between lower frequencies, streaks are located downstream, while for higher frequency interactions, streaks are located upstream. Streaks are formed in the regions where the frequencies are active. We extend Ellingsen and Palm [50]'s work to include nonlinearities and find that the nonlinear term plays a significant role in the intensity of streaks. This nonlinear term is comparable in magnitude to the linear production term but has the opposite sign, suggesting that nonlinearities extract energy from streaks.

Interaction maps were employed to explore the spatial distribution of nonlinear interactions across various triads. It was found that for interactions involving lower azimuthal wavenumbers, nonlinear activity congregates near the end of the potential core, whereas for those with higher azimuthal wavenumbers, it concentrates in the shear layer closer to the nozzle exit. Similarly, nonlinear activity is observed upstream for higher-frequency interactions and downstream for lower-frequency interactions. Moreover, a local analysis was conducted to pinpoint the most dominant azimuthal triads at different streamwise locations, revealing a transition from [12,-6,6] at $x = 1$ to [2,-1,1] at $x = 5$, and settling

11

at [2,2,4] beyond $x = 10$. By computing the nonlinear transfer term, the direction of energy transfer was identified, revealing an inverse energy cascade in the initial shear layer and a forward energy cascade downstream of the potential core. These findings hold intriguing implications for flow control, suggesting that by suppressing the inverse energy cascade in the shear layer, it is possible to diminish the energy of lower azimuthal components, such as $m = 1$ and 2, potentially leading to a reduction in radiated sound.

References

[1] Jordan, P., and Colonius, T., "Wave packets and turbulent jet noise," *Annu. Rev. Fluid Mech.*, Vol. 45, 2013, pp. 173–195.

[2] Crow, S. C., and Champagne, F. H., "Orderly structure in jet turbulence," *J. Fluid Mech.*, Vol. 48, No. 3, 1971, pp. 547–591.

[3] Michalke, A., "Instability of a compressible circular free jet with consideration of the influence of the jet boundary layer thickness," 1977.

[4] Crighton, D. G., and Gaster, M., "Stability of slowly diverging jet flow," *J. Fluid Mech.*, Vol. 77, No. 2, 1976, pp. 397–413.

[5] Tam, C. K., and Morris, P. J., "The radiation of sound by the instability waves of a compressible plane turbulent shear layer," *J. Fluid Mech.*, Vol. 98, No. 2, 1980, pp. 349–381. https://doi.org/10.1017/S0022112080000195.

[6] Tam, C. K., and Burton, D. E., "Sound generated by instability waves of supersonic flows. Part 1. Two-dimensional mixing layers," *J. Fluid Mech.*, Vol. 138, 1984, pp. 249–271. https://doi.org/10.1017/S0022112084000112.

[7] Crighton, D. G., and Huerre, P., "Shear-layer pressure fluctuations and superdirective acoustic sources," *J. Fluid Mech.*, Vol. 220, 1990, pp. 355–368.

[8] Towne, A., Schmidt, O. T., and Colonius, T., "Spectral proper orthogonal decomposition and its relationship to dynamic mode decomposition and resolvent analysis," *J. Fluid Mech.*, Vol. 847, 2018, pp. 821–867.

[9] Schmidt, O. T., Towne, A., Rigas, G., Colonius, T., and Brès, G. A., "Spectral analysis of jet turbulence," *J. Fluid Mech.*, Vol. 855, 2018, pp. 953–982.

[10] Cavalieri, A. V. G., Rodríguez, D., Jordan, P., Colonius, T., and Gervais, Y., "Wavepackets in the velocity field of turbulent jets," *J. Fluid Mech.*, Vol. 730, 2013, pp. 559–592.

[11] Kraichnan, R. H., "Inertial ranges in two-dimensional turbulence," *The Physics of Fluids*, Vol. 10, No. 7, 1967, pp. 1417–1423.

[12] Kraichnan, R. H., "Inertial-range transfer in two-and three-dimensional turbulence," *J. Fluid Mech.*, Vol. 47, No. 3, 1971, pp. 525–535.

[13] Waleffe, F., "The nature of triad interactions in homogeneous turbulence," *Physics of Fluids A: Fluid Dynamics*, Vol. 4, No. 2, 1992, pp. 350–363.

[14] Yeh, T. T., and Van Atta, C. W., "Spectral transfer of scalar and velocity fields in heated-grid turbulence," *J. Fluid Mech.*, Vol. 58, No. 2, 1973, pp. 233–261.

[15] Lii, K. S., Rosenblatt, M., and Van Atta, C., "Bispectral measurements in turbulence," *J. Fluid Mech.*, Vol. 77, No. 1, 1976, pp. 45–62.

[16] Kim, Y. C., and Powers, E. J., "Digital bispectral analysis and its applications to nonlinear wave interactions," *IEEE transactions on plasma science*, Vol. 7, No. 2, 1979, pp. 120–131.

[17] Herring, J. R., "Theoretical calculations of turbulent bispectra," *J. Fluid Mech.*, Vol. 97, No. 1, 1980, pp. 193–204.

[18] Schmidt, O. T., "Bispectral mode decomposition of nonlinear flows," *Nonlinear dynamics*, Vol. 102, No. 4, 2020, pp. 2479–2501.

[19] Goparaju, H., and Gaitonde, D. V., "Role of entropic instabilities in laminar-turbulent transition on a blunted flat plate," *Phys. Rev. Fluids*, Vol. 7, No. 10, 2022, p. 103901.

[20] Sousa, C. E., Kennedy, R. E., King, R. A., Bathel, B. F., Weisberger, J. M., and Laurence, S. J., "Global analysis of nonlinear second-mode development in a Mach-6 boundary layer from high-speed schlieren data," *Experiments in Fluids*, Vol. 65, No. 2, 2024, pp. 1–22.

[21] Maia, I., Jordan, P., Heidt, L., Colonius, T., Nekkanti, A., and Schmidt, O. T., "Nonlinear dynamics of forced wavepackets in turbulent jets," *AIAA Aviation 2021 Forum*, 2021, p. 2277.

[22] Nekkanti, A., Maia, I. A., Jordan, P., Heidt, L., Colonius, T., and Schmidt, O. T., "Triadic nonlinear interactions and acoustics of forced versus unforced turbulent jets," *12th International Symposium on Turbulence and Shear Flow Phenomena (TSFP12). Osaka, Japan*, 2022.

[23] Nekkanti, A., Schmidt, O. T., Maia, I., Jordan, P., Heidt, L., and Colonius, T., "Bispectral mode decomposition of axisymmetrically and non-axisymmetrically forced turbulent jets," *AIAA Aviation 2023 Forum*, 2023, p. 3651.

[24] Moczarski, L., Treleaven, N. C., Oberleithner, K., Schmidt, S., Fischer, A., and Kaiser, T. L., "Interaction of multiple linear helical modes in the turbulent flow field of an industrial fuel injection system," *AIAA SciTech 2022 Forum*, 2022, p. 1061.

[25] Moczarski, L., Treleaven, N. C. W., Oberleithner, K., Schmidt, S., Fischer, A., and Kaiser, T. L., "Interacting Linear Modes in the Turbulent Flow of an Industrial Swirled Combustor," *AIAA J.*, Vol. 62, No. 3, 2024, pp. 979–988.

[26] Nekkanti, A., Nidhan, S., Schmidt, O. T., and Sarkar, S., "Large-scale streaks in a turbulent bluff body wake," *J. Fluid Mech.*, Vol. 974, 2023, p. A47.

[27] Patel, H. D., and Yeh, C. A., "Modal analysis for three-dimensional instability coupling mechanisms in turbulent wake flows over an airfoil," *AIAA SCITECH 2023 Forum*, 2023, p. 1987.

[28] Hajj, M., Miksad, R., and Powers, E., "Subharmonic growth by parametric resonance," *J. Fluid Mech.*, Vol. 236, 1992, pp. 385–413.

[29] Husain, H., and Hussain, F., "Experiments on subharmonic resonance in a shear layer," *J. Fluid Mech.*, Vol. 304, 1995, pp. 343–372.

[30] Paschereit, C., Wygnanski, I., and Fiedler, H., "Experimental investigation of subharmonic resonance in an axisymmetric jet," *J. Fluid Mech.*, Vol. 283, 1995, pp. 365–407.

[31] Cohen, J., and Wygnanski, I., "The evolution of instabilities in the axisymmetric jet. Part 1. The linear growth of disturbances near the nozzle," *J. Fluid Mech.*, Vol. 176, 1987, pp. 191–219.

[32] Wu, X., and Huerre, P., "Low-frequency sound radiated by a nonlinearly modulated wavepacket of helical modes on a subsonic circular jet," *J. Fluid Mech.*, Vol. 637, 2009, pp. 173–211.

[33] Long, T. A., and Petersen, R. A., "Controlled interactions in a forced axisymmetric jet. Part 1. The distortion of the mean flow," *J. Fluid Mech.*, Vol. 235, 1992, pp. 37–55.

[34] Reynolds, W. C., Parekh, D. E., Juvet, P. J. D., and Lee, M. J. D., "Bifurcating and blooming jets," *Annu. Rev. Fluid Mech.*, Vol. 35, No. 1, 2003, pp. 295–315.

[35] Broze, G., and Hussain, F., "Nonlinear dynamics of forced transitional jets: periodic and chaotic attractors," *J. Fluid Mech.*, Vol. 263, 1994, pp. 93–132.

[36] Broze, G., and Hussain, F., "Transitions to chaos in a forced jet: intermittency, tangent bifurcations and hysteresis," *J. Fluid Mech.*, Vol. 311, 1996, pp. 37–71.

[37] Brès, G. A., and Lele, S. K., "Modeling of Jet Noise – A perspective from Large-Eddy Simulations," *Phil. Trans. Royal Soc. A*, Vol. Accepted for publication, No. xxx, 2019.

[38] Brès, G. A., Ham, F. E., Nichols, J. W., and Lele, S. K., "Unstructured large-eddy simulations of supersonic jets," *AIAA J.*, 2017, pp. 1164–1184.

[39] Brès, G. A., Jordan, P., Jaunet, V., Le Rallic, M., Cavalieri, A. V. G., Towne, A., Lele, S. K., Colonius, T., and Schmidt, O. T., "Importance of the nozzle-exit boundary-layer state in subsonic turbulent jets," *J. Fluid Mech.*, Vol. 851, 2018, pp. 83–124.

[40] Pope, S. B., "Turbulent flows,", 2001.

[41] Schmidt, O. T., and Colonius, T., "Guide to spectral proper orthogonal decomposition," *AIAA J.*, Vol. 58, No. 3, 2020, pp. 1023–1033.

[42] Nekkanti, A., and Schmidt, O. T., "Frequency–time analysis, low-rank reconstruction and denoising of turbulent flows using SPOD," *J. Fluid Mech.*, Vol. 926, 2021, p. A26. https://doi.org/10.1017/jfm.2021.681.

[43] Nekkanti, A., and Schmidt, O. T., "Gappy spectral proper orthogonal decomposition," *J. Comput. Phys.*, Vol. 478, 2023, p. 111950.

[44] Heidt, L., and Colonius, T., "Optimal frequency resolution for spectral proper orthogonal decomposition," *arXiv preprint arXiv:2402.15775*, 2024.

[45] Schmidt, O. T., Towne, A., Rigas, G., Colonius, T., and Brès, G. A., "Spectral analysis of jet turbulence," *J. Fluid Mech.*, Vol. 855, 2018, pp. 953–982.

[46] Tissot, G., Zhang, M., Lajús, F. C., Cavalieri, A. V. G., and Jordan, P., "Sensitivity of wavepackets in jets to nonlinear effects: the role of the critical layer," *J. Fluid Mech.*, Vol. 811, 2017, pp. 95–137.

[47] Benney, D. J., "A non-linear theory for oscillations in a parallel flow," *J. Fluid Mech.*, Vol. 10, No. 2, 1961, pp. 209–236.

[48] Pierrehumbert, R. T., and Widnall, S. E., "The two-and three-dimensional instabilities of a spatially periodic shear layer," *J. Fluid Mech.*, Vol. 114, 1982, pp. 59–82.

[49] Pickering, E., Rigas, G., Nogueira, P. A. S., Cavalieri, A. V. G., Schmidt, O. T., and Colonius, T., "Lift-up, Kelvin–Helmholtz and Orr mechanisms in turbulent jets," *J. Fluid Mech.*, Vol. 896, 2020.

[50] Ellingsen, T., and Palm, E., "Stability of linear flow," *Phys. Fluids*, Vol. 18, No. 4, 1975, pp. 487–488.

[51] Landahl, M. T., "A note on an algebraic instability of inviscid parallel shear flows," *J. Fluid Mech.*, Vol. 98, No. 2, 1980, pp. 243–251.

[52] Brandt, L., "The lift-up effect: the linear mechanism behind transition and turbulence in shear flows," *European Journal of Mechanics-B/Fluids*, Vol. 47, 2014, pp. 80–96.

[53] Nogueira, P. A. S., Cavalieri, A. V. G., Jordan, P., and Jaunet, V., "Large-scale, streaky structures in turbulent jets," *J. Fluid Mech.*, Vol. 873, 2019, pp. 211–237.

[54] Sasaki, K., Cavalieri, A. V. G., Jordan, P., Schmidt, O. T., Colonius, T., and Brès, G. A., "High-frequency wavepackets in turbulent jets," *J. Fluid Mech.*, Vol. 830, 2017.

[55] Nekkanti, A., and Schmidt, O. T., "Modal analysis of acoustic directivity in turbulent jets," *AIAA J.*, Vol. 59, No. 1, 2021, pp. 228–239.

[56] Brissaud, A., Frisch, U., Léorat, J., Lesieur, M., and Mazure, A., "Helicity cascades in fully developed isotropic turbulence," *Physics of Fluids*, Vol. 16, No. 8, 1973, pp. 1366–1367.

[57] Biferale, L., Musacchio, S., and Toschi, F., "Inverse energy cascade in three-dimensional isotropic turbulence," *Physical review letters*, Vol. 108, No. 16, 2012, p. 164501.

[58] Alexakis, A., and Biferale, L., "Cascades and transitions in turbulent flows," *Physics Reports*, Vol. 767, 2018, pp. 1–101.

[59] Plunian, F., Teimurazov, A., Stepanov, R., and Verma, M. K., "Inverse cascade of energy in helical turbulence," *J. Fluid Mech.*, Vol. 895, 2020, p. A13.